

# Toggle-like current-induced Bloch point dynamics of 3D skyrmion strings in a room-temperature nanowire

Max Birch (✉ [m.t.birch@durham.ac.uk](mailto:m.t.birch@durham.ac.uk))

Max Planck Institute for Intelligent Systems <https://orcid.org/0000-0001-9320-8561>

David Cortés-Ortuño

Department of Earth Sciences, Utrecht University

Kai Litzius

Massachusetts Institute of Technology <https://orcid.org/0000-0002-6408-2581>

Sebastian Wintz

Max Planck Institute for Intelligent Systems

Frank Schulz

Max Planck Institute for Intelligent Systems

Markus Weigand

Helmholtz-Zentrum Berlin für Materialien und Energie, Albert-Einstein-Str. 15, 12489

<https://orcid.org/0000-0002-0325-2268>

Aleš Štefančič

Electrochemistry Laboratory, Paul Scherrer Institut

Daniel Mayoh

Department of Physics, University of Warwick

Geetha Balakrishnan

Department of Physics <https://orcid.org/0000-0002-5890-1149>

Peter Hatton

Durham University <https://orcid.org/0000-0002-7651-3393>

Gisela Schütz

MPI Metallforschung

---

Letter

Keywords:

Posted Date: January 10th, 2022

DOI: <https://doi.org/10.21203/rs.3.rs-1235546/v1>

**License:**  This work is licensed under a Creative Commons Attribution 4.0 International License.

[Read Full License](#)

---

**Version of Record:** A version of this preprint was published at Nature Communications on June 24th, 2022. See the published version at <https://doi.org/10.1038/s41467-022-31335-y>.

# **Toggle-like current-induced Bloch point dynamics of 3D skyrmion strings in a room temperature nanowire**

M. T. Birch<sup>1</sup>, D. Cortés-Ortuño<sup>2</sup>, K. Litzius<sup>1</sup>, S. Wintz<sup>1,3</sup>, F. Schulz<sup>1</sup>, M. Weigand<sup>3</sup>, Aleš Štefančíč<sup>4,6</sup>, D. A. Mayoh<sup>4</sup>, G. Balakrishnan<sup>4</sup>, P. D. Hatton<sup>5</sup>, G. Schütz<sup>1</sup>

<sup>1</sup>*Max Planck Institute for Intelligent Systems, 70569 Stuttgart, Germany*

<sup>2</sup>*Department of Earth Sciences, Utrecht University, 3584 CB Utrecht, The Netherlands*

<sup>3</sup>*Helmholtz-Zentrum Berlin für Materialien und Energie GmbH, 12489 Berlin, Germany*

<sup>4</sup>*Department of Physics, University of Warwick, Coventry, CV4 7AL, UK*

<sup>5</sup>*Department of Physics, Durham University, Durham DH1 3LE, UK*

<sup>6</sup>*Current Institution: Electrochemistry Laboratory, Paul Scherrer Institut, CH-5232 Villigen PSI, Switzerland*

1 **Research into practical applications of magnetic skyrmions, nanoscale solitons with inter-**  
2 **esting topological and transport properties<sup>1,2</sup>, has traditionally focused on two dimensional**  
3 **(2D) thin-film systems<sup>3,4</sup>. However, the recent observation of novel three dimensional (3D)**  
4 **skyrmion-like structures, such as hopfions<sup>5</sup>, skyrmion strings (SkS)<sup>6-9</sup>, skyrmion bundles<sup>11</sup>,**  
5 **and skyrmion braids<sup>12</sup>, motivates the investigation of new designs, aiming to exploit the third**  
6 **spatial dimension for more compact and higher performance spintronic devices in 3D or**  
7 **curvilinear geometries<sup>13-15</sup>. A crucial requirement of such device schemes is the control of**  
8 **the 3D magnetic structures via charge or spin currents, which has yet to be experimentally**  
9 **observed. In this work, we utilise real-space imaging to investigate the dynamics of a 3D**  
10 **SkS within a nanowire of  $\text{Co}_8\text{Zn}_9\text{Mn}_3$  at room temperature. Utilising single, nanoscale cur-**  
11 **rent pulses, we demonstrate current-induced nucleation of a single SkS, and a toggle-like**  
12 **positional switching of an individual Bloch point at the end of a SkS. The observations high-**  
13 **light the possibility to locally manipulate 3D topological spin textures, opening up a range of**  
14 **design concepts for future 3D spintronic devices.**

15 In systems with broken inversion symmetry and the presence of strong spin-orbit coupling,  
16 the interplay of the Dzyaloshinskii-Moriya interaction (DMI) with the exchange interaction results  
17 in the formation of monochiral spin textures, including magnetic skyrmions<sup>16</sup>. In 2D thin film  
18 systems, the symmetry-breaking proximity of heavy metal and ferromagnetic layers induces an  
19 interfacial DMI, resulting in the formation of Néel-type skyrmions<sup>3,4</sup>, which are inherently limited  
20 in vertical size by the film thickness. On the other hand, in bulk chiral magnets, the broken in-  
21 version symmetry of the underlying crystal structure results in a bulk DMI<sup>17</sup>, and the formation of

22 extended SkSs, which could conceptually extend through the thickness of a single crystal<sup>18,19</sup>.

23 The extended vertical structure of a SkS was only recently identified in real-space in B20  
24 chiral magnets<sup>6-8</sup>, and subsequently via 3D tomographic imaging<sup>9,10</sup>. These SkS structures exhibit  
25 fascinating dynamical properties. Firstly, their formation and annihilation mechanisms are gov-  
26 erned by topological defects known as Bloch points<sup>18,19</sup>. The motion of these emergent magnetic  
27 monopoles acts as a source or sink of topological charge, mediating the creation of 3D topologi-  
28 cal structures from trivial magnetic states<sup>20,21</sup>. Secondly, recent studies investigating the resonant  
29 and singular spinwave dynamics of SkSs have demonstrated the transmission of signals along  
30 the length of a SkS over length scales of 50  $\mu\text{m}$ <sup>22,23</sup>, indicating their potential use as nanoscale  
31 magnonic transmission lines<sup>24</sup>.

32 Moreover, exotic 3D magnetic objects with higher order topologies have recently been ob-  
33 served, such as the magnetic hopfion<sup>5</sup> or bound states composed of multiple SkSs in the form  
34 of skyrmion bundles<sup>11</sup>, and skyrmion braids<sup>12</sup>. The potential to devise and assemble dynamic  
35 structures using these complex topological states in 3D or curvilinear geometries is a fascinating  
36 possibility, with the potential to realise improved spintronic device designs<sup>13-15</sup>. While current-  
37 induced motion and writing of individual skyrmions has been demonstrated for 2D skyrmions<sup>25,26</sup>,  
38 such control has yet to be observed for 3D topological structures. Therefore, we identified a com-  
39 pelling need to explore the possibility of controlling and manipulating 3D SkS states in device-like  
40 geometries.

41 In this work, we utilise scanning transmission x-ray microscopy (STXM) to investigate the

42 stability of SkS states in a nanowire of  $\text{Co}_8\text{Zn}_9\text{Mn}_3$  at room temperature. We find that SkSs within  
43 the confined nanowire shape appear to be more stable than in plate-like lamellae samples. Further-  
44 more, we demonstrate current-induced generation and local manipulation of an individual SkS, in  
45 the form of toggle-like switching of the SkS length. The results demonstrate the potential of future  
46 3D skyrmion-based device schemes, and motivate further exploration to control the rich dynamics  
47 of 3D topological magnetic structures.

48 Using a focused ion beam, we fabricated a nanowire with dimensions  $5000 \times 700 \times 200$   
49 nm from a single crystal of  $\text{Co}_8\text{Zn}_9\text{Mn}_3$ , a bulk chiral magnet with a measured Curie temperature,  
50  $T_C$ , of  $\sim 360 \text{ K}^{29}$  (magnetometry characterisation and wire geometry shown in Extended Data  
51 Fig. 1). The sample was fixed to gold contacts patterned on a  $\text{Si}_3\text{N}_4$  membrane, allowing current  
52 to be applied along its length. A schematic illustration and a scanning electron micrograph of  
53 the fabricated device is shown in Fig. 1a and b, respectively. A controllable quadrupole magnet  
54 allowed the field to be applied either in the OOP or IP directions, respectively along the thickness  
55 ( $z$ -axis) and width ( $y$ -axis) of the wire, as indicated in Fig. 1a. We utilised an additional resistive  
56 wire attached to the sample holder, enabling heating, and subsequent zero-field cooling (ZFC) or  
57 field-cooling (FC), of the nanowire.

58 Scanning transmission x-ray microscopy (STXM) was utilised to image the spin textures on  
59 the nanoscale. Magnetic contrast was achieved by exploiting the effects of XMCD at the resonant  
60 absorption Co  $L_3$  edge at 779 eV, producing a signal proportional to  $m_z$  (see methods, Extended  
61 Data Fig. 1). We identified four magnetic states within the nanowire: the helical state, formed after

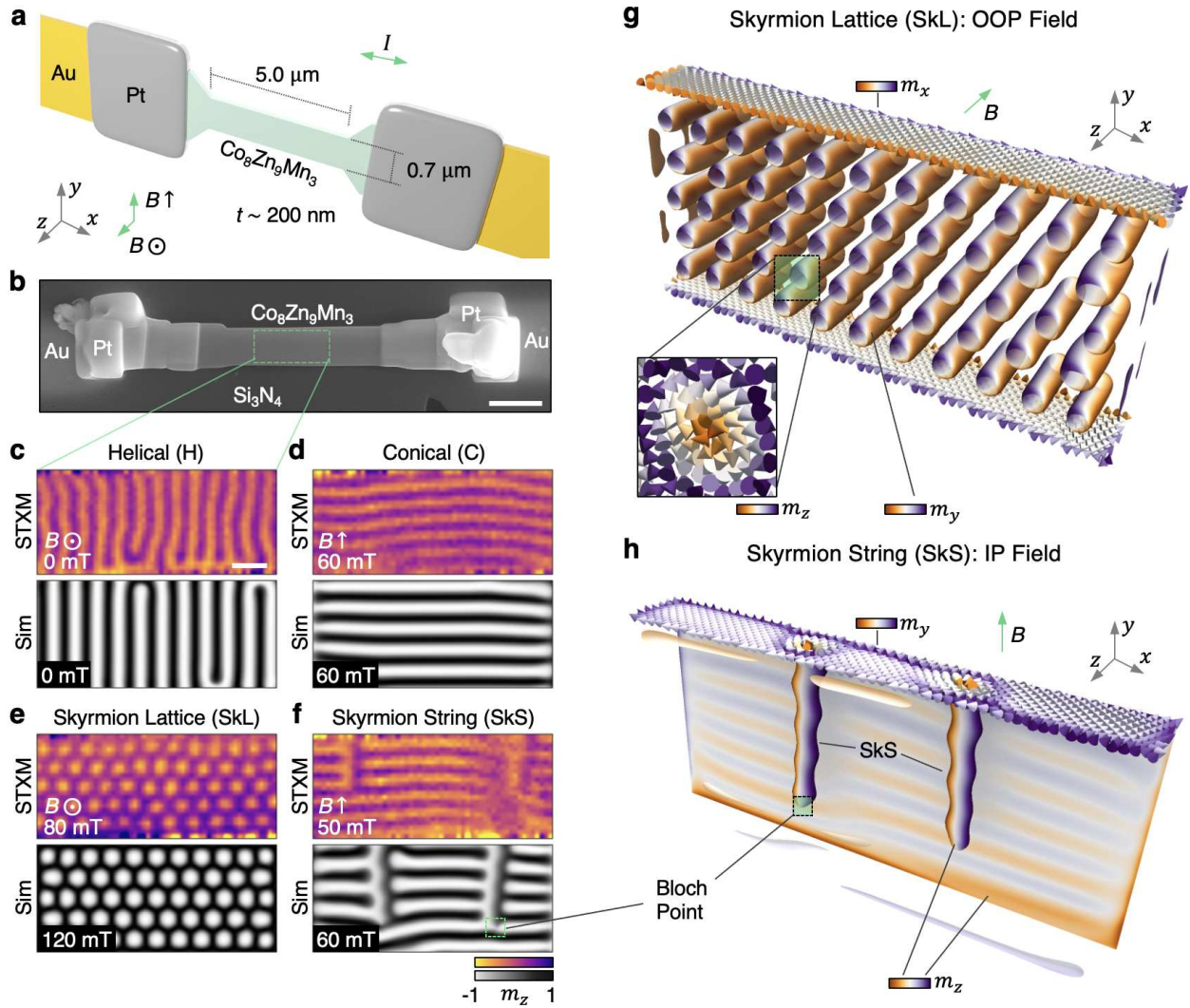


Figure 1 |  **$\text{Co}_8\text{Zn}_9\text{Mn}_3$  nanowire and observed chiral spin textures.** **a**, Schematic illustration of the device construction, showing the  $\text{Co}_8\text{Zn}_9\text{Mn}_3$  nanowire on the  $\text{Si}_3\text{N}_4$  membrane, fixed by platinum (Pt) deposition welds to the patterned gold (Au) contacts. The orientation of the out-of-plane (OOP,  $B \odot$ ) and in-plane (IP,  $B \uparrow$ ) applied field configurations is indicated. **b**, Scanning electron microscopy image of the final device. The scale bar is 1  $\mu\text{m}$ . **c-f**, Scanning transmission x-ray microscopy (STXM) and simulated (Sim) images of the helical (H), conical (C), skyrmion lattice (SkL) and skyrmion string (SkS) states, as observed in the nanowire. The colourmap indicates the out-of-plane magnetisation component,  $m_z$ , and the scale bar is 250 nm. **g,h**, Three dimensional visualisations of the simulated skyrmion lattice and skyrmion string states, realised with OOP and IP applied fields respectively. The colourmap specifies the local orientation of the magnetisation, as indicated by the labels. The inset shows the local spin structure of the skyrmions in **g**.

62 ZFC, with its winding vector  $k$ , of length 120 nm, aligned along the  $x$ -axis (Fig. 1c); the conical  
63 state, realised by applying an IP field, with winding length 120 nm and  $k$  along the  $y$ -axis (Fig. 1d);  
64 the SkL state, produced after FC with an OOP field, showing its characteristic hexagonal structure  
65 with a lattice spacing of 148 nm (Fig. 1e); and finally the SkS state, produced after FC with an  
66 IP field (Fig. 1f). The two SkSs can be identified by the light and dark vertical contrast lines,  
67 corresponding to the Bloch-type chirality, embedded within the horizontal contrast lines of the  
68 background conical state<sup>6</sup>. Their observation upon FC indicates that the SkSs were created within  
69 the equilibrium skyrmion phase close to  $T_C$  during the cooling procedure, and quenched to low  
70 temperatures, forming a metastable state<sup>30,31</sup>. For each STXM image, a comparable micromagnetic  
71 simulation is shown, demonstrating a strong agreement with the experimentally observed states  
72 (see methods). Visualisations of the SkL and SkS state simulations are shown in Fig. 1g and  
73 h respectively, highlighting the Bloch-type chiral structure of the skyrmions, and indicating the  
74 locations of the Bloch points at the termination points of the SkSs<sup>19</sup>.

75 We explored the formation and stability of these chiral states within the confined nanowire by  
76 acquiring images as a function of increasing applied field for both OOP and IP orientation, starting  
77 at  $-250$  mT. The results are summarised in the single-temperature phase diagrams in Fig. 2a and  
78 b. For the OOP configuration, the helical state at 0 mT is transformed into isolated skyrmions at  
79 higher fields. In contrast, for an IP field, the helical state rotates to form the conical state, before  
80 reaching a uniformly magnetised (UM), saturated state above 100 mT. Fig. 2c displays the states  
81 realised after FC at different applied IP fields. When cooling within the range of 40 to 80 mT, we  
82 reproducibly achieved SkS states embedded within the conical background. The same SkS state

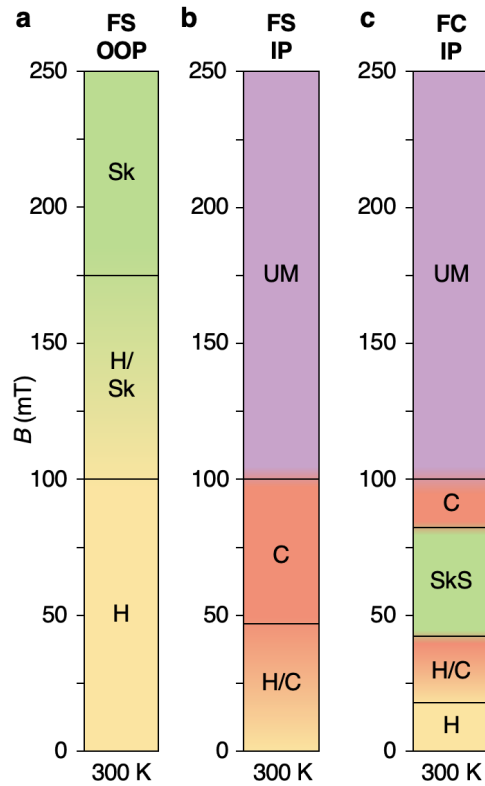


Figure 2 | **Room temperature magnetic phase diagrams.** **a-c**, Diagrams indicating the magnetic state exhibited by the sample as a function of the applied magnetic field when following different measurement protocols: performing a field sweep (FS,  $-250$  to  $250$  mT) with an out-of-plane (OOP) magnetic field (**a**), performing a FS with an in-plane (IP) magnetic field (**b**), and finally when field cooling (FC) at a range of IP magnetic fields (**c**). Labels indicate the formation of the helical (H), conical (C), skyrmion lattice (SkL), skyrmion string (SkS) and uniformly magnetised (UM) spin textures.

83 was observed to remain intact after 12 hours, indicating the formation of long-lived metastable  
84 SkSs<sup>30,31</sup>. The images utilised to create these diagrams are shown in Extended Data Figs 2-4.

85 Having achieved SkS states within the wire, we explored their stability against both increas-  
86 ing and decreasing applied magnetic field. Fig. 3a displays a STXM image of two adjacent SkSs  
87 within the conical background. When applying an increasing magnetic field, the conical state con-  
88 trast disappeared, and the SkSs were shortened, demonstrating the topological unwinding process  
89 as the Bloch point travelled along their length, as shown in Fig. 3b and c. Finally, at 110 mT,  
90 the SkS were reduced to a length comparable to the winding length of the material, indicating the  
91 formation of two chiral bobbbers<sup>32</sup>. Therefore, the image in Fig. 3d presents a side-on perspective  
92 of these topological surface states. Fig. 3e-h display simulated images of comparable magnetic  
93 states, confirming the identity of the observed SkS and chiral bobber states.

94 We performed similar measurements for decreasing magnetic field, starting with a state con-  
95 sisting of two separated SkSs, as shown in Fig. 3i-l. For decreasing field, the SkSs annihilate into  
96 the conical/helical background by the formation of a dislocation, as shown in the case of the left  
97 SkS in Fig. 3k. Finally, the SkSs are totally annihilated into a mixed conical and helical state,  
98 shown in Fig. 3l. Once again, the simulated images in Fig. 3m-p demonstrate a comparable  
99 behaviour in the micromagnetic system (experimental data set and 3D visualisations of the simu-  
100 lations presented in Extended Data Figs 5-7). Both high-field unwinding and low-field dislocation  
101 annihilation mechanisms are mediated by the formation of Bloch point structures<sup>18,19,21</sup>. The pres-  
102 ence of these diverging magnetisation points is shown in the 3D visualisations of the simulations

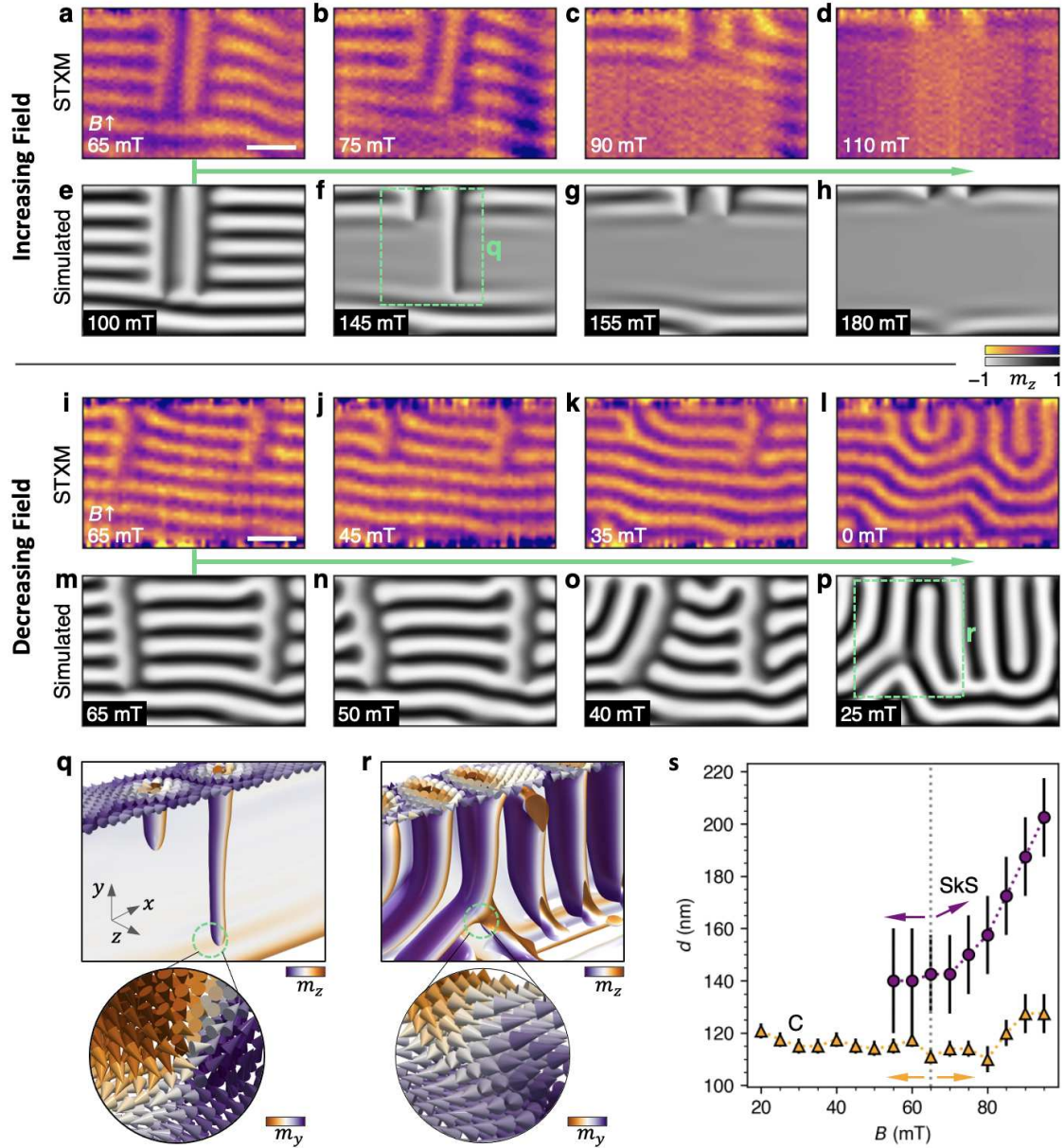


Figure 3 | **Field stability of the skyrmion string spin texture in a nanowire geometry.** **a-p**, X-ray microscopy images (**a-d,i-l**) and simulated images (**e-h,m-p**) of the skyrmion string (SkS) spin texture as a function of increasing (**a-h**), and decreasing (**i-p**) in-plane (IP) applied magnetic field, as indicated by the green arrows. The colourmap indicates the out-of-plane magnetisation component,  $m_z$ . The scale bar is 250 nm. **q, r**, Three dimensional visualisation of the simulations in **f** and **p** respectively. The insets show a visualisation of the local spin structure at the end point of the SkS (**q**), and at the formation point of a dislocation (**r**), highlighting the diverging magnetisation indicating the presence of a Bloch point. **s**, The experimentally determined spacing  $d$  of the SkS and conical (C) states as a function of the applied field. The dotted line and arrows show the initial point and direction of the field sweep. Error bars indicate the error calculated due to the resolution limit, and the averaged number of measured SkS/C spacings.

103 presented in Fig. 3q and r.

104 In addition to the strong agreement of the simulated states with the experimental images,  
105 another key identifying property of the SkS state is their spacing  $d$  as a function of the applied  
106 magnetic field. In particular, the spacing of the SkSs should increase as a function of the applied  
107 field<sup>6</sup>, whereas the helical and stripe domain states remain at the characteristic winding length  
108 of the system, in this case 120 nm. The spacing of the observed conical and SkS states was  
109 determined by acquiring line profiles of the experimental images (examples shown in Extended  
110 Data Fig. 9), and plotted in Fig. 3s. The larger, field dependent spacing of the vertical contrast  
111 structures confirms their identity as SkS states.

112 Due to shape anisotropy and confinement effects, the dimensions of the host system play a  
113 crucial role in the stability of skyrmion states. Plate-like lamellae samples dramatically increase the  
114 stability of the skyrmion lattice (SkL) state for out-of-plane (OOP) fields, extending the equilibrium  
115 phase pocket down to lower temperatures far below  $T_C$ <sup>28</sup>. However, our previous results indicated  
116 that for in-plane (IP) fields, the resulting in-plane extended SkS states appeared to be less stable in  
117 lamellae than in bulk<sup>6</sup>. The present measurements highlight the wide range of fields over which  
118 the SkS remains stable within the nanowire, demonstrating the potential suitability of SkSs for use  
119 in confined, device-like geometries.

120 The possibility to realise current-induced dynamics in the nanowire device was investigated  
121 by applying bipolar pulses with a 30 ns duration (15 ns positive current pulse, followed immedi-  
122 ately by 15 ns negative current pulse) to single SkS states, as shown in Fig. 4a-j. Bipolar pulses

123 were use to negate any overall current-induced motion of the SkSs along the nanowire. In each  
124 case, the current density transmitted through the nanowire during the pulse was estimated to be  
125  $5.9 \times 10^{10}$  A/m<sup>2</sup> (see methods). Fig. 4a-e exhibits an example where an additional SkS was nu-  
126 cleated adjacent to the initial SkS via single pulses. Interestingly, before reaching this state, the  
127 system formed a dislocation within the conical background in the vicinity of the original SkS,  
128 which was observed to relax back to the conical state with time. This excited state perhaps forms  
129 as an intermediary state on the way to SkS nucleation. Further measurements showed that SkS  
130 states could be reproducibly generated from an initial conical state by a series of 100 of the same  
131 30 ns bipolar current pulses (full data set shown in Extended Data Fig. 8). In a second example,  
132 shown in Fig. 4f-j, we found it was possible to alter the length of the SkS between 3 and 4 conical  
133 lengths,  $L_C$ , with individual pulses of the same current density. This observation therefore repre-  
134 sents a current-induced toggle-like switching of the position of an individual Bloch point at the end  
135 of the SkS.

136 To determine the origin of these dynamic effects, we measured the amplitude of the reflected  
137 and output (transmitted through the sample) signals as a function of the input pulse amplitude, as  
138 shown by the example trace in Fig. 4k. These measurements enable calculation of the resistance of  
139 the sample as a function of the input current density (see methods). Together with a calibration of  
140 the sample resistance as a function of temperature, this quantifies the change in sample temperature  
141 due to the Joule heating effect (more example traces and calibration shown in Extended Data Figure  
142 10). The resulting plot of temperature change versus current density in Fig. 4l indicates a heating  
143 of less than 10 K for the highest amplitude pulses, which is still 40 K below the measured value of

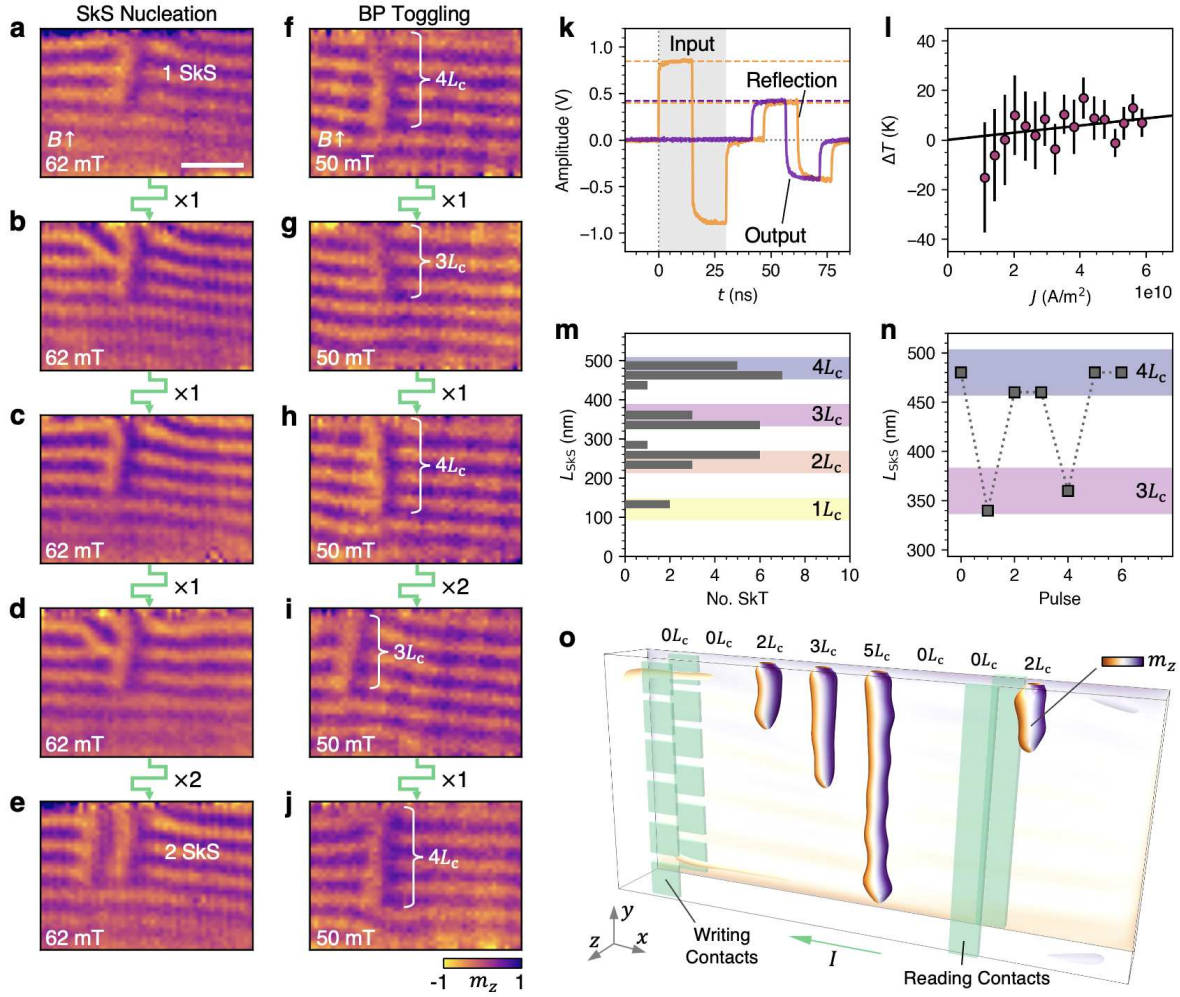


Figure 4 | **Current-induced dynamics of the skyrmion string spin texture at room temperature.** **a-e**, X-ray microscopy images of the nanowire sample, showing the magnetic state following bipolar 15 ns pulses with a current density of  $6 \times 10^{10}$  A/m<sup>2</sup>, showing the initial single skyrmion string (SkS) state, followed by the formation of conical dislocations and finally a second SkS. The number of pulses between each image is indicated. **f-g**, Images of the nanowire sample, showing the magnetic state following bipolar 15 ns pulses of  $6 \times 10^{10}$  A/m<sup>2</sup>. Successive pulses show alteration of the SkS length between a 3-4 $L_c$ . **k**, The amplitude of the bipolar pulse trace as a function of time, showing the input, reflected and output signals. By measuring the pulse traces for a range of input amplitudes, the resistance of the sample can be calculated, and the temperature change due to Joule heating can be estimated. **l**, The estimated change in temperature of the sample due to Joule heating as a function of current density  $J$ , suggesting a  $\Delta T < 10$  K. **m**, A histogram showing the measured lengths of SkSs observed within the nanowire sample. Coloured regions indicate integer values of  $L_c$ , suggesting that the length of the SkS is a quantised integer of  $L_c$ . **n**, The length of the SkS in **f-j** after each consecutive pulse, showing the toggle-like switching of the Bloch point position located at the end of the SkS. **o**, An illustration of an example 3D skyrmion racetrack device concept, exploiting the quantised length of the SkS as a data storage element.

144  $T_C$ . Importantly, this is an upper bound estimate of the Joule heating effect, since the calculation  
145 assumes that all of the energy was dissipated within the nanowire, whereas in reality heating will  
146 also occur within the contact bonds and cables. Therefore, we conclude that a Joule heating effect  
147 is likely not a significant factor in the present results, indicating that the observed dynamics are  
148 due to some current-induced effect. We note that the current density of  $5.9 \times 10^{10}$  A/m<sup>2</sup> utilised  
149 to observe the SkS generation and dynamics here is comparable to current induced motion of 2D  
150 skyrmions within lamellae of Co-Zn-Mn alloys<sup>27</sup>, and one or two orders of magnitude lower than  
151 in examples of skyrmion dynamics within thin-film sputtered systems<sup>4</sup>.

152 The toggle-like motion of the Bloch point indicated that the length of the skyrmion string is  
153 in some way quantised to an integer value of the conical length,  $L_C$ . To investigate this further, we  
154 measured the length of the observed SkS states, and plotted their occurrence as a histogram, shown  
155 in Fig. 4m. One can see that the majority of the SkS states were close to integer lengths of  $L_C$ , as  
156 indicated by the coloured bands. Similarly, the length of the SkS following each current pulse in  
157 Fig. 4f-j is plotted in Fig. 4n, highlighting the toggle-like switching of the Bloch point position by  
158 120 nm. We speculate that this apparent quantisation may occur when it is energetically favourable  
159 for the Bloch point to sit at a specific position within the background conical state, perhaps due  
160 to the symmetry breaking of magnetocrystalline or shape anisotropy. For SkSs existing within a  
161 uniformly magnetised background, we anticipate that such an effect would not be observed.

162 We envisage that this toggle-like switching of individual Bloch points, demonstrated here at  
163 room temperature, could have interesting applications in future 3D skyrmion devices utilising SkS

164 states. In Fig. 4o, we present a generalisation of the skyrmion racetrack device concept<sup>33</sup> from  
165 2D to 3D, which could exploit the quantisation of the SkS length within the conical background  
166 to store data in the third dimension. A current along the  $x$ -axis would translate the SkSs along the  
167 wire, as in a typical racetrack design. Individual writing contacts applying current across the  $z$ -axis  
168 could take advantage of the observed current-induced Bloch point motion to set the length of the  
169 SkSs. A second pair of contacts could measure the magnitude of skyrmion Hall effect across the  
170 thickness of the wire to read out the length of the stored SkS state.

171 In summary, the present results feature the reproducible formation of long-lived SkS states  
172 within a nanowire geometry at room temperature. Furthermore, we demonstrate both single-pulse,  
173 current-induced generation of a single SkS, and local manipulation of the SkS texture in the form  
174 of toggle-like positional switching of an individual Bloch point located at the end of the SkS.  
175 Our analysis confirms that the observed dynamics are most likely current-induced, rather than due  
176 to Joule heating effects. In the future, we anticipate intensive research into the manipulation of  
177 further 3D topological spin textures beyond SkSs, including magnetic hopfions, skyrmion bundles  
178 and skyrmion strings, with the view to realise advanced 3D spintronic device architectures.

## 179 **Methods**

180 **Sample fabrication and characterisation.** Crystals of  $\text{Co}_8\text{Zn}_9\text{Mn}_3$  were grown via the Bridgman  
181 method. Stoichiometric amounts of Co powder (Alfa-Aesar, 99.99%), Zn powder (SigmaAldrich,  
182 99.995%) and Mn pieces (Alfa-Aesar, 99.99%) were ground together and transferred to an alumina  
183 crucible with a pointed end, and sealed inside an evacuated quartz tube. The tube was then heated

184 to 1060 °C and allowed to homogenize for 12 hours. It was then slowly cooled at a rate of 1 °C/hr  
185 to 700 °C and left to anneal for several days at this temperature before being water quenched.  
186 Single crystals of  $\text{Co}_8\text{Zn}_9\text{Mn}_3$  were isolated from the as-grown boule and oriented using X-ray  
187 Laue back-reflection.

188 Magnetometry measurements were carried out using an MPMS3 vibrating sample magne-  
189 tometer, equipped with the AC susceptibility option. A combination of photolithography and mag-  
190 netron sputtering was performed to pattern  $\sim 200$  nm thick gold contacts onto a  $\text{Si}_3\text{N}_4$  membrane  
191 suitable for transmission measurements. Using a focused ion beam, a thin lamella of material was  
192 fabricated using a typical lift-out method. This lamella was milled into a nanowire shape with  
193 dimensions of  $0.7 \times 0.2 \times 5$   $\mu\text{m}$ . The nanowire was then positioned over the gold contacts on the  
194 membrane using an in-situ micromanipulator, and fixed in place with localised platinum deposition.

195 **Scanning transmission x-ray microscopy.** Scanning transmission x-ray microscopy measure-  
196 ments were carried out at the MAXYMUS endstation at the BESSY II electron storage ring op-  
197 erated by the Helmholtz-Zentrum Berlin für Materialien und Energie. The sample was fixed and  
198 bonded to the sample holder, and a resistive wire was attached close to the sample to allow for rapid  
199 local heating. With the sample mounted inside the vacuum chamber, the applied magnetic field  
200 was achieved by altering the orientation of four permanent magnets. Field-cooling was achieved  
201 by applying  $\sim 10$  seconds of continuous 1 A current to the resistive wire, which resulted in the  
202 temperature of the sample rising above  $T_C$ , enabling the FC and ZFC procedures to be performed  
203 in-situ. Using a Fresnel zone plate and order selecting aperture, the x-ray beam was focused to a  
204  $\sim 20$  nm spot size. To acquire an image, the sample was rastered through the x-ray focal point

205 using a piezoelectric motor stage, measuring the transmission pixel by pixel. Magnetic contrast  
206 was achieved by tuning the x-ray energy to the Co L<sub>3</sub> edge at 779 eV, exploiting the resonant ab-  
207 sorption effects of x-ray circular dichroism<sup>34</sup>. This results in the absorption of the x-rays changing  
208 proportionally to the local out-of-plane magnetisation of the sample,  $m_z$ . A schematic illustration  
209 of the technique and an example XMCD spectrum are presented in Extended Data Fig. 1h. All  
210 presented STXM images are the result of dividing two images acquired with positive and negative  
211 x-ray circular polarisation, eliminating all structural contrast and leaving only the XMCD magnetic  
212 contrast. The photon count was measured by an avalanche photodiode. A typical image required  
213 10 minutes of measurement time for each polarisation.

214 Bipolar current pulses were applied to the sample contacts using the two output channels  
215 of an Agilent Technologies 81134A pulse generator. The traces of the output and input pulses  
216 were recorded using a pickoff T and a Teledyne Lecroy waverunner 8404, such that the signal  
217 transmission through the sample could be measured. For the measurements shown in the main  
218 text, we applied a 15 ns pulse from each input channel, with the second channel inverted, resulting  
219 in a bipolar pulse with a total length of 30 ns and an input pulse amplitude of 0.9 V. For these  
220 values, the transmitted output pulse was measured to be 0.41 V measured over the 50  $\Omega$  resistance  
221 at the oscilloscope. This corresponds to a current density through the nanowire of  $5.9 \times 10^{10}$  A/m<sup>2</sup>.  
222 For the multi-pulse excitations, where SkSs were nucleated using a series of 100 pulses, the pulse  
223 separation was set to 60  $\mu$ s – a suitable length to prevent compound heating of the sample from  
224 successive current pulses.

225 A key result of the work is that the observed SkS dynamics are current-induced rather than

226 due to Joule heating effects. To determine this, the change in resistance of the sample,  $R_s$ , within  
227 the x-ray microscope was determined by applying a series of current pulses with input amplitude,  
228  $V_{in}$ , between 0.1 and 0.9 V, corresponding to current densities between  $1.1 \times 10^{10}$  and  $5.9 \times 10^{10}$   
229  $A/m^2$ , and by measuring the amplitude of the reflected and output pulses,  $V_{ref}$  and  $V_{out}$ , respectively.  
230 Any increase in sample temperature due to Joule heating would result in an increase in the sample  
231 resistance. The resistance can be calculated following the equation<sup>35</sup>,

$$R_s = \frac{V_{in} + V_{ref} - V_{out}}{V_{out}} \cdot 50 \Omega. \quad (1)$$

232 We then performed a separate resistance versus temperature calibration of the sample on a hot  
233 plate, measured by a Keithley 2450 sourcemeter and thermocouple. Utilising this calibration,  
234 we converted the change in the sample resistance to a change in the sample temperature as a  
235 function of the input pulse current density,  $J$ . Example pulse traces and the resistance-temperature  
236 calibration are shown in Extended Data Fig. 10. The analysis indicates that the upper bound for  
237 the temperature change of the nanowire due to the current pulses was less than 10 K. However,  
238 this estimate assumes that all of the Joule heating is dissipated within the nanowire itself, while  
239 in reality an unknown fraction of the energy will be lost within the contact bonds and cables.  
240 Therefore, we concluded that there was likely no significant Joule heating effect within the system  
241 for the applied pulse parameters, and certainly not enough to raise the sample to  $T_C$ .

242 **Micromagnetic Simulations** Simulations of the SkS states were performed using the micromag-  
243 netic finite difference code MuMax3<sup>36</sup> and data was processed using the OOMMFPy library<sup>37</sup>.  
244 In the continuum, the cubic chiral-lattice magnet  $Co_9Zn_9Mn_2$ , with space group  $P4_132$ , can be

245 described by the energy functional

$$E = \int_V dV \left\{ A \sum_{\alpha=x,y,z} (\nabla m_\alpha)^2 + D \mathbf{m} \cdot (\nabla \times \mathbf{m}) - M_s \mathbf{m} \cdot \mathbf{B} - \frac{M_s}{2} \mathbf{m} \cdot \mathbf{B}_d \right\}, \quad (2)$$

246 where  $\mathbf{m}$  is the normalised magnetisation field,  $A$  is the exchange constant,  $M_s$  is the saturation  
247 magnetisation,  $D$  is the DMI constant,  $\mathbf{B}$  is the applied field and  $\mathbf{B}_d$  is the demagnetising field,  
248 including the shape anisotropy of the wire. Thus, the terms within the equation represent the  
249 exchange, DMI, Zeeman and demagnetisation energies. The magnetic parameters were adjusted  
250 to match the helical lengths observed in the experiments. Specifically, from the dc magnetization  
251 data of  $\text{Co}_8\text{Zn}_9\text{Mn}_3$  reported by Bocarsly et al.<sup>38</sup> a saturation magnetization for a cubic lattice of  
252  $M_s = 460.55$  kA/m was utilised. Additionally, optimal magnitudes for the exchange and DMI to  
253 obtain a helical length of 120 nm were determined by simulating SkS states at different magnetic  
254 field strengths, increasing  $D$  from an initial value reported by Takagi et al. for  $\text{Co}_9\text{Zn}_9\text{Mn}_2$ <sup>39</sup>. As  
255 a result, the exchange and DMI constants were found to be  $A = 5.729$  pJ/m and  $D = 0.6$  mJ/m<sup>2</sup>,  
256 respectively.

257 The sample was simulated using a rectangular region with dimensions comparable to the  
258 experimental system,  $5 \times 0.7 \times 0.2$   $\mu\text{m}$ , which was discretised using cubic cells of 5 nm edge  
259 length – slightly below the exchange length of the material with a value of 6.56 nm. In order to  
260 obtain the SkS states with a Bloch point at their end, initial states based on a paraboloid function  
261 were specified, as in our previous work<sup>6</sup>, and the energy was minimised using a combination of  
262 the Landau-Lifshitz-Gilbert equation and the steepest descent method. To observe the helical state  
263 propagating across the length of the sample as observed in the experiment (rather than across the  
264 width), a small anisotropy of 4 kJ/m<sup>3</sup> magnitude with a hard axis along the  $x$ -axis was included.

265 Simulations using a cubic anisotropy did not show this magnetic configuration. For the simulation  
266 of a skyrmion lattice, an initial state based on the magnetization function was used with the helical  
267 length of  $\text{Co}_8\text{Zn}_9\text{Mn}_3$ <sup>40</sup>. Differences in the applied field values between the simulated and exper-  
268 imental systems can likely be explained due to the temperature effects, where the micromagnetic  
269 system is essentially modelled at zero temperature.

270 **Data Availability** Experimental and simulation data, and the relevant analysis scripts utilised to  
271 produce the presented figures are available from an online repository<sup>41</sup> (not yet available). Further  
272 material is available from the corresponding authors upon reasonable request.

- 274 1. Nagaosa, N. & Tokura, Y. Topological properties and dynamics of magnetic skyrmions. *Nat.*  
275 *Nanotechnol.* **8**, 899 (2013).
- 276 2. Back, C., *et al.* The 2020 skyrmionics roadmap. *J. Phys. D: Appl. Phys.* **53**, 363001 (2020).
- 277 3. Moreau-Luchaire, C. *et al.* Additive interfacial chiral interaction in multilayers for stabilization  
278 of small individual skyrmions at room temperature. *Nat. Nanotechnol.* **11**, 444–448 (2016).
- 279 4. Woo, S. *et al.* Observation of room-temperature magnetic skyrmions and their current-driven  
280 dynamics in ultrathin metallic ferromagnets. *Nat. Mater.* **15**, 501–506 (2016).
- 281 5. Kent, N. *et al.* Creation and observation of Hopfions in magnetic multilayer systems. *Nat. Com-*  
282 *mun.* **12**, 1562 (2021).
- 283 6. Birch, M. T. *et al.* Real-space imaging of confined magnetic skyrmion tubes. *Nat. Commun.* **11**,  
284 1726 (2020).

- 285 7. Yu, X. *et al.* Real-Space Observation of Topological Defects in Extended Skyrmion-Strings.  
286 *Nano Lett.* **20**, 7313–7320 (2020).
- 287 8. Mathur, N. *et al.* In-plane magnetic field-driven creation and annihilation of magnetic skyrmion  
288 strings in nanostructures. *Adv. Funct. Mater.* **31**, 2008521 (2021).
- 289 9. Seki, S. *et al.* Direct visualization of the three-dimensional shape of skyrmion strings in a non-  
290 centrosymmetric magnet. *Nat. Mater.* <https://doi.org/10.1038/s41563-021-01141-w> (2021).
- 291 10. Wolf, D. *et al.* Unveiling the three-dimensional magnetic texture of skyrmion tubes. *Nat. Nan-*  
292 *otechnol.* <https://doi.org/10.1038/s41565-021-01031-x> (2021).
- 293 11. Tang, J. *et al.* Magnetic skyrmion bundles and their current-driven dynamics. *Nat. Nanotech-*  
294 *nol.* **16**, 1086-1091 (2021).
- 295 12. Zheng, F. *et al.* Magnetic skyrmion braids. *Nat. Commun.* **12**, 5316 (2021).
- 296 13. Fernández-Pacheco, A. *et al.* Three-dimensional nanomagnetism. *Nat. Commun.* **8**, 15756  
297 (2017).
- 298 14. Fischer, P., Sanz-Hernández, D., Streubel, R. & Fernández-Pacheco, A. Launching a new  
299 dimension with 3D magnetic nanostructures. *APL Mater.* **8**, 010701 (2020)
- 300 15. Makarov, D. *et al.* New Dimension in Magnetism and Superconductivity: 3D and Curvilinear  
301 Nanoarchitectures. *Adv. Mater.* 2101758 (2021).
- 302 16. Rößler, U. K., Bogdanov, A. N. & Pfleiderer, C. Spontaneous skyrmion ground states in mag-  
303 netic metals. *Nature* **442**, 797 (2006).

- 304 17. Mühlbauer, S. *et al.* Skyrmion Lattice in a Chiral Magnet. *Science* **323**, 915 (2009).
- 305 18. Milde, P., *et al.* Unwinding of a Skyrmion Lattice by Magnetic Monopoles. *Science* **340**, 1076  
306 (2013).
- 307 19. Kagawa, F. *et al.* Current-induced viscoelastic topological unwinding of metastable skyrmion  
308 strings. *Nat. Commun.* **8**, 1332 (2017).
- 309 20. Schütte, C. & Rosch, A. Dynamics and energetics of emergent magnetic monopoles in chiral  
310 magnets. *Phys. Rev. B* **90**, 174432 (2014).
- 311 21. Birch, M. T. *et al.* Topological defect-mediated skyrmion annihilation in three dimensions.  
312 *Communications Physics* **4**, 175 (2021).
- 313 22. Seki, S. *et al.* Propagation dynamics of spin excitations along skyrmion strings. *Nat. Commun.*  
314 **11**, 256 (2020).
- 315 23. Kravchuk, V. P. *et al.* Solitary wave excitations of skyrmion strings in chiral magnets. *Phys.*  
316 *Rev. B* **102**, 220408(R) (2020).
- 317 24. Xing, X., Zhou, Y. & Braun, H. B. Skyrmion Tubes as Magnonic Waveguides. *Phys. Rev.*  
318 *Applied* **13**, 034051 (2020).
- 319 25. Woo, S. *et al.* Deterministic creation and deletion of a single magnetic skyrmion observed by  
320 direct time-resolved X-ray microscopy. *Nat. Electron.* **1**, 288–296 (2018).
- 321 26. Yu, X. *et al.* Motion tracking of 80-nm-size skyrmions upon directional current injections. *Sci.*  
322 *Adv.* **6**, eaaz9744 (2020).

- 323 27. Peng, L. *et al* Dynamic transition of current-driven single-skyrmion motion in a room-  
324 temperature chiral-lattice magnet. *Nat. Commun.* **12**, 6797 (2021).
- 325 28. Yu, X. Z. *et al*. Near room-temperature formation of a skyrmion crystal in thin-films of the  
326 helimagnet FeGe. *Nat. Mater.* **10**, 106 (2011).
- 327 29. Tokunaga, Y. *et al*. A new class of chiral materials hosting magnetic skyrmions beyond room  
328 temperature. *Nat. Commun.* **6**, 7638 (2015).
- 329 30. Münzer, W. *et al*. Skyrmion lattice in the doped semiconductor  $\text{Fe}_{1-x}\text{Co}_x\text{Si}$ . *Phys. Rev. B* **81**,  
330 041203(R) (2010).
- 331 31. Karube, K. *et al*. Robust metastable skyrmions and their triangular-square lattice structural  
332 transition in a high-temperature chiral magnet. *Nat. Mat.* **15**, 1237 (2016).
- 333 32. Zheng, F. *et al*. Experimental observation of chiral magnetic bobbars in B20-type FeGe. *Nat.*  
334 *Nanotechnol.* **13**, 451–455 (2018).
- 335 33. Tomasello, R. *et al*. A strategy for the design of skyrmion racetrack memories. *Sci. Rep.* **4**,  
336 6784 (2015).

## 337 **Methods References**

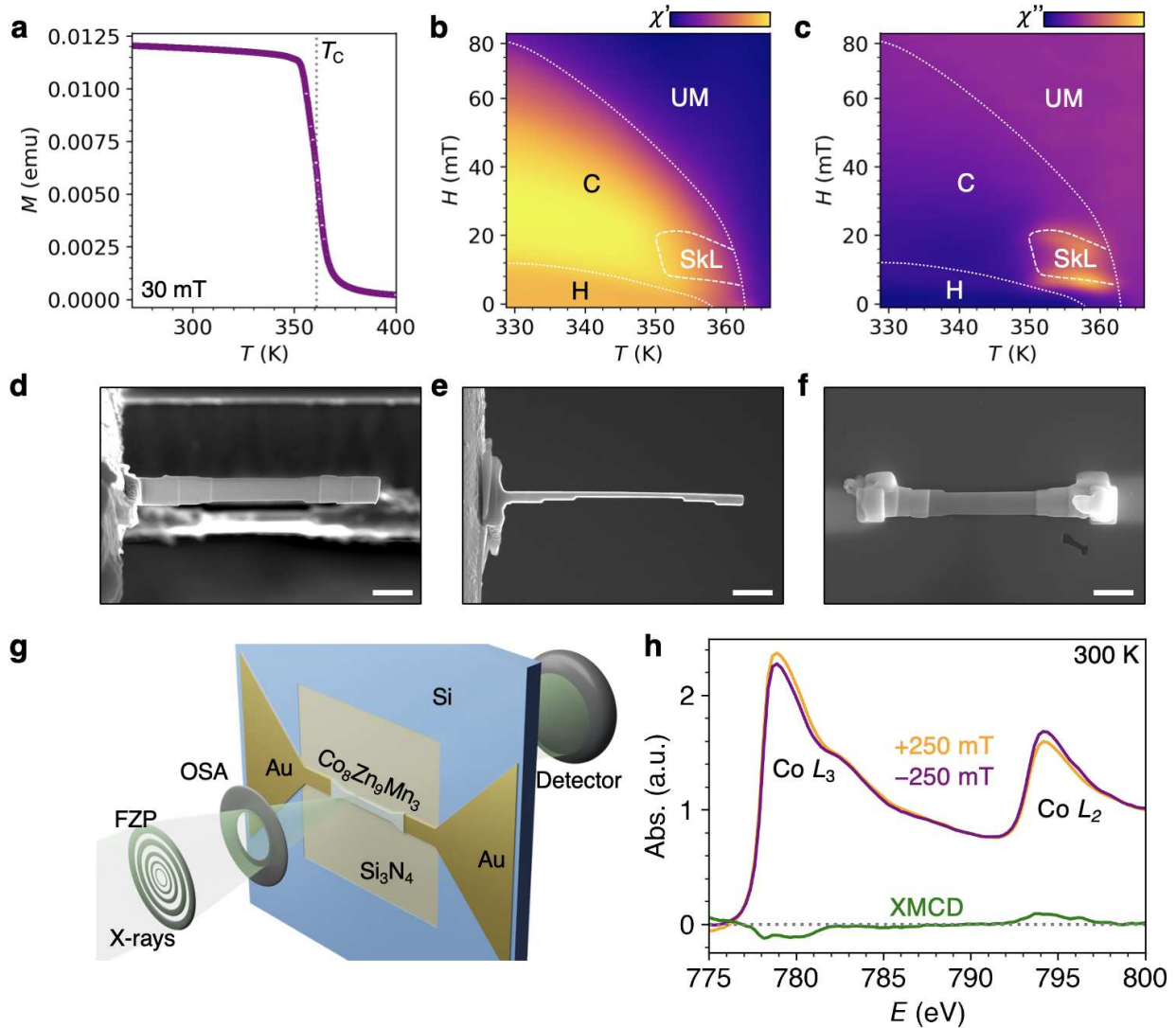
- 338 34. van der Laan, G. & Figuerao, A. I. X-ray magnetic circular dichroism — A versatile tool to  
339 study magnetism. *Coord. Chem. Rev.* **277**, 95-129 (2014).
- 340 35. Litzius, K. *et al.* The role of temperature and drive current in skyrmion dynamics. *Nat. Elec-*  
341 *tron.* **3**, 30-36 (2020).
- 342 36. Vansteenkiste, A. The design and verification of MuMax3. *AIP Advances* **4**, 107133 (2014).
- 343 37. Cortés-Ortuño, D. OOMMFPy Python module. doi: 10.5281/zenodo.2611194 (2019).
- 344 38. Bocarsly, J. D. *et al.* Deciphering structural and magnetic disorder in the chiral skyrmion host  
345 materials  $\text{Co}_x\text{Zn}_y\text{Mn}_z$  ( $x + y + z = 20$ ). *Phys. Rev. Materials* **3**, 014402 (2019).
- 346 39. Takagi, R. *et al.* Spin-wave spectroscopy of the Dzyaloshinskii-Moriya interaction in room-  
347 temperature chiral magnets hosting skyrmions. *Phys. Rev. B* **95**, 220406(R) (2017).
- 348 40. Lancaster, T. *et al.* Transverse field muon-spin rotation signature of the skyrmion-lattice phase  
349 in  $\text{Cu}_2\text{OSeO}_3$ . *Phys. Rev. B* **91**, 224408 (2015).
- 350 41. Birch, M. T & Cortés-Ortuño, D. Online data repository. Not yet available (2021).

351 **Acknowledgements** The authors acknowledge the support of A. C. Harrison and U. Eigenthaler for advice  
352 on the focused ion beam fabrication. We thank the Helmholtz-Zentrum für Materialien und Energie for the  
353 allocation of synchrotron beamtime under proposal 202-10087-ST. The work was partially funded by the  
354 UK Skyrmion Project EPSRC Programme Grant (EP/N032128/1).

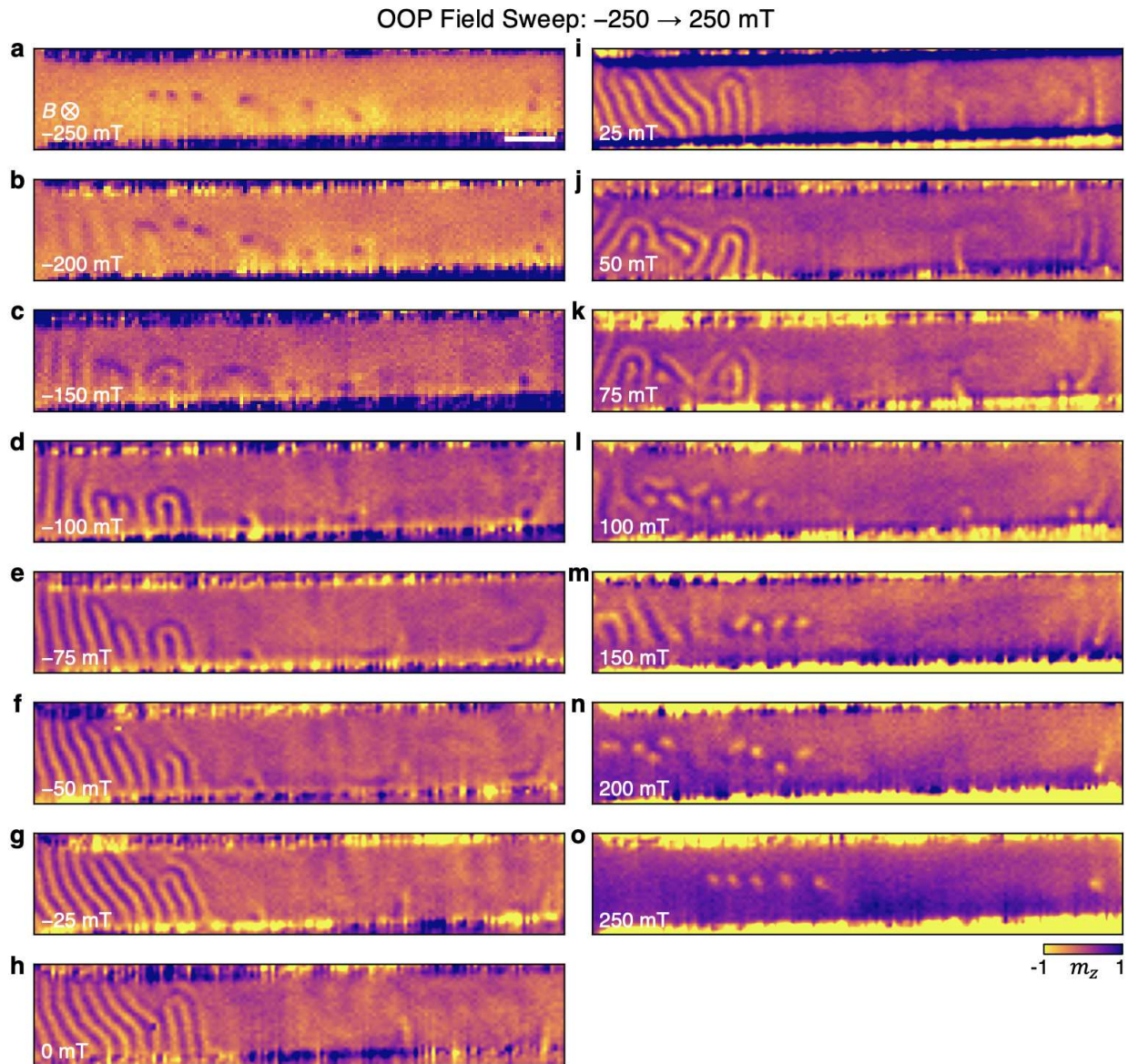
355 **Author Contributions** MTB, PDH and GS conceived the project. AS, DAM and GB fabricated the bulk  
356 sample. MTB fabricated the nanowire device structure. MTB, KL, SW, FS and MW performed the x-  
357 ray imaging measurements. MTB and KL conducted the current pulse measurements and analysis. DC-  
358 O carried out the micromagnetic simulations. MTB and DC-O wrote the manuscript with input from all  
359 authors. All authors discussed the results and gave feedback on the manuscript.

360 **Competing Interests** The authors declare no competing interests.

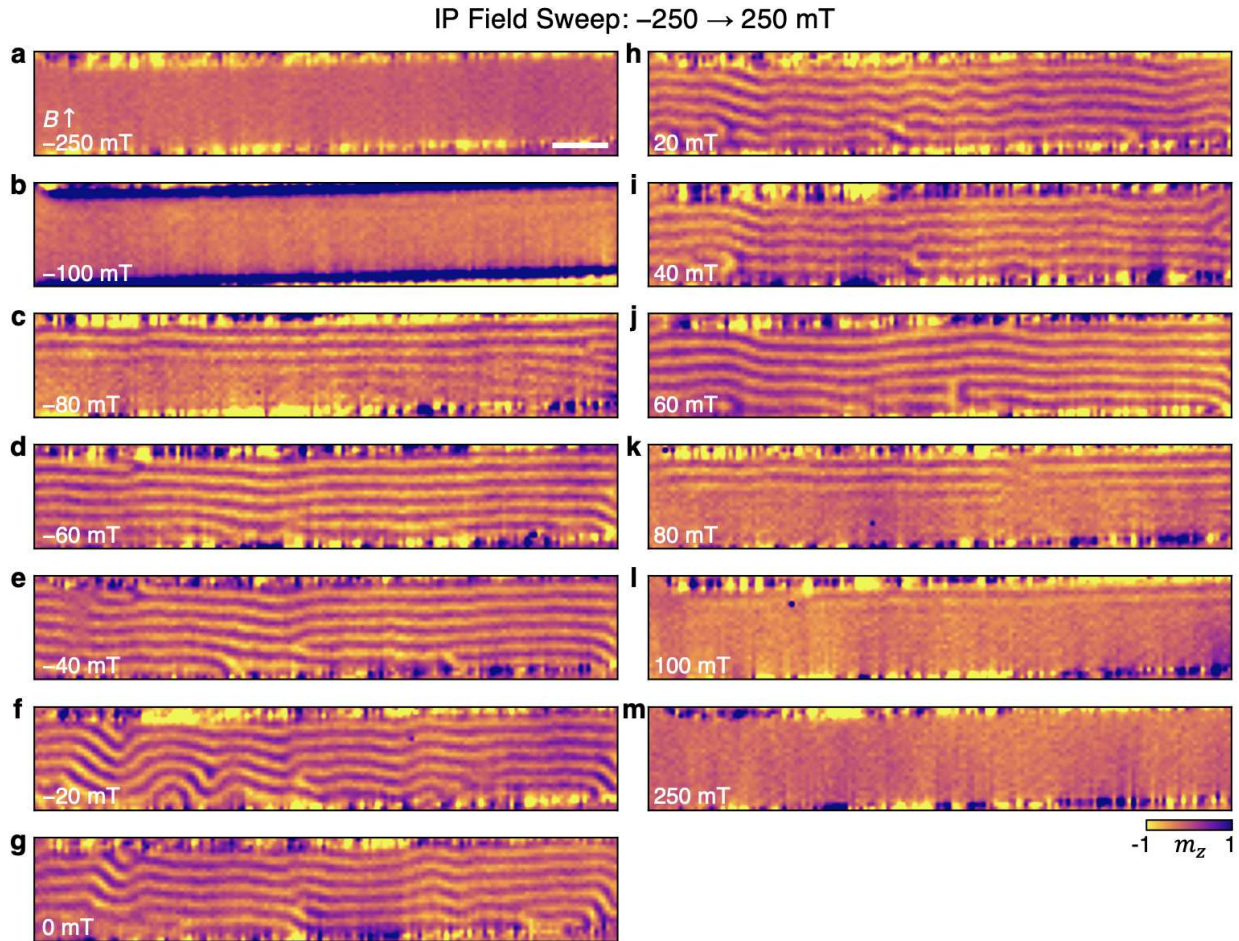
361 **Correspondence** Correspondence and requests for materials should be addressed to M. T. Birch and D.  
362 Cortés-Ortuño (email: birch@is.mpg.de, david.cortes.o@gmail.com).



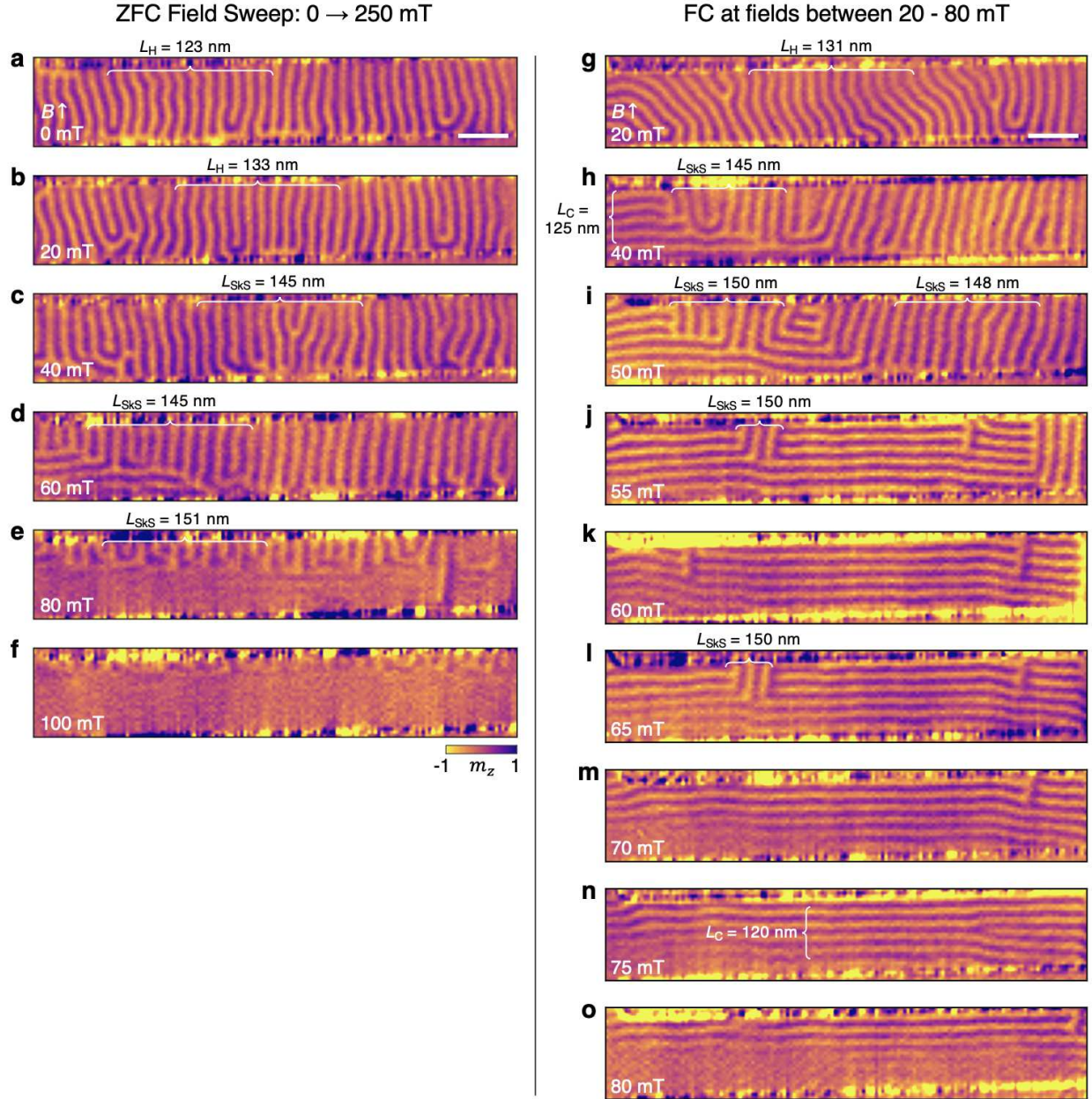
Extended Data Figure 1 | **Bulk sample characterisation and nanowire fabrication.** **a**, Magnetisation,  $M$ , measured as a function of decreasing temperature,  $T$ , on the bulk  $\text{Co}_8\text{Zn}_9\text{Mn}_3$  single crystal sample under an applied magnetic field of 30 mT. The measured  $T_C$  is  $\sim 361$  K. **b,c**, The real and imaginary components of the AC susceptibility,  $\chi'$  and  $\chi''$  respectively, measured with the single crystal, as a function of increasing field  $B$  at each temperature. The boundaries separating the helical (H), conical (C), uniformly magnetised (UM) and equilibrium skyrmion lattice (SkL) states are indicated. **d-f**, Scanning electron microscopy images of the nanowire sample as it was fabricated (**d,e**), and after being fixed to the gold (Au) contacts on the  $\text{Si}_3\text{N}_4$  membrane (**f**). The scale bar is 1  $\mu\text{m}$ . **g**, Schematic illustration of scanning transmission x-ray microscopy technique, where the incoming x-rays are focused to a  $\sim 20$  nm spot size by a Fresnel zone plate (FZP) and order selecting aperture (OSA). Transmitted photons are counted by the photodiode detector. **h**, The absorption of the nanowire sample measured as a function of x-ray energy  $E$  across the Co  $L_3$  and  $L_2$  edges. By measuring for applied out-of-plane magnetic fields of  $\pm 250$  mT, and subtracting the two datasets, the x-ray magnetic circular dichroism (XMCD) signal is revealed (green).



Extended Data Figure 2 | **Out-of-plane magnetic field sweep.** **a-o**, Scanning transmission x-ray microscopy images of the  $\text{Co}_8\text{Zn}_9\text{Mn}_3$  nanowire sample, acquired as a function of increasing out-of-plane field starting from  $-250$  mT. The colourmap indicates the out-of-plane magnetisation  $m_z$ . This data was utilised to create the single temperature phase diagram in Fig. 2a of the main text. The scale bar is 500 nm.

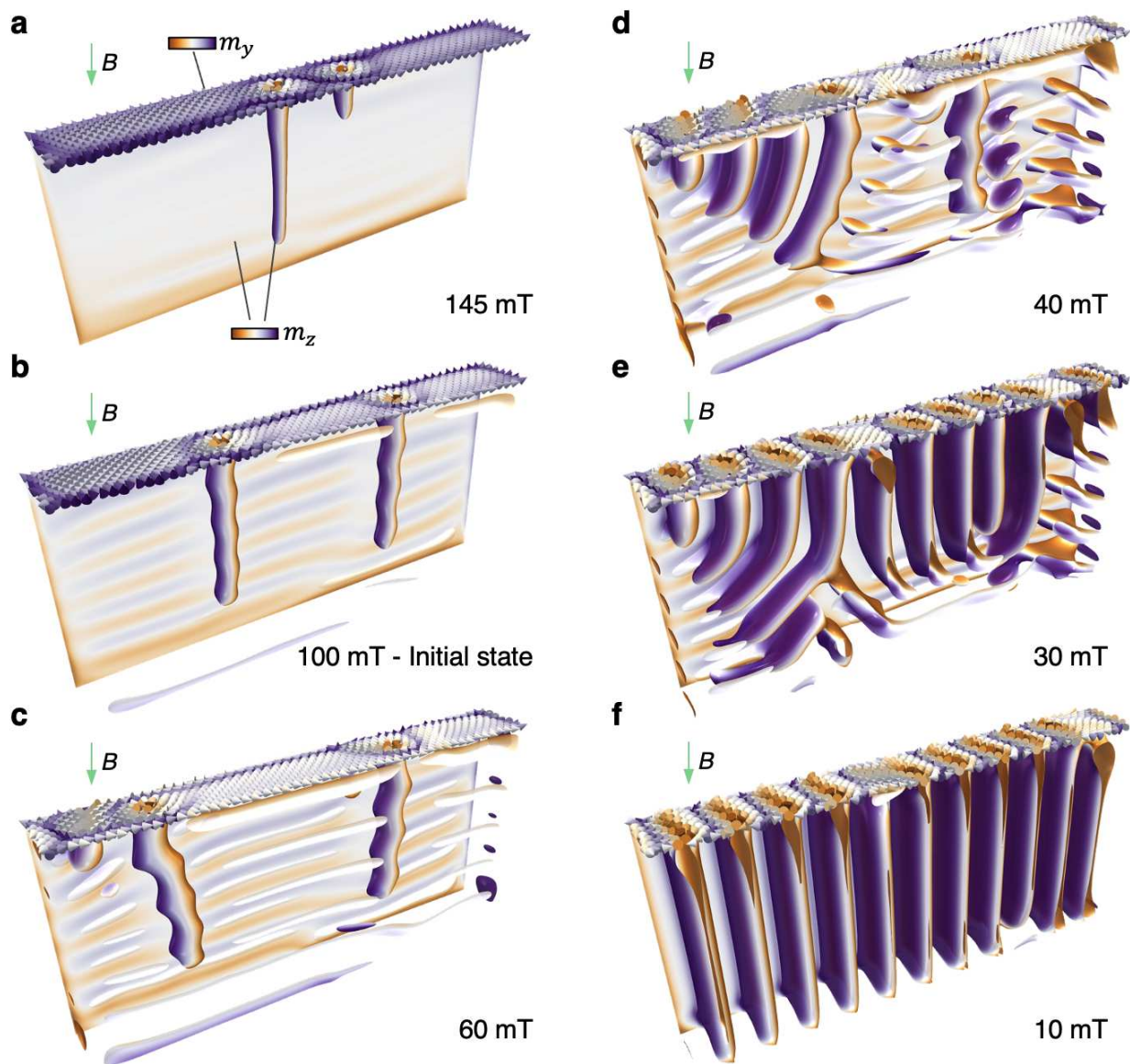


Extended Data Figure 3 | **In-plane magnetic field sweep.** **a-m**, Scanning transmission x-ray microscopy images of the nanowire sample, acquired as a function of increasing in-plane field starting from  $-250$  mT. The colourmap indicates the out-of-plane magnetisation  $m_z$ . This data was utilised to create the single temperature phase diagram in Fig. 2b of the main text. The scale bar is  $500$  nm.

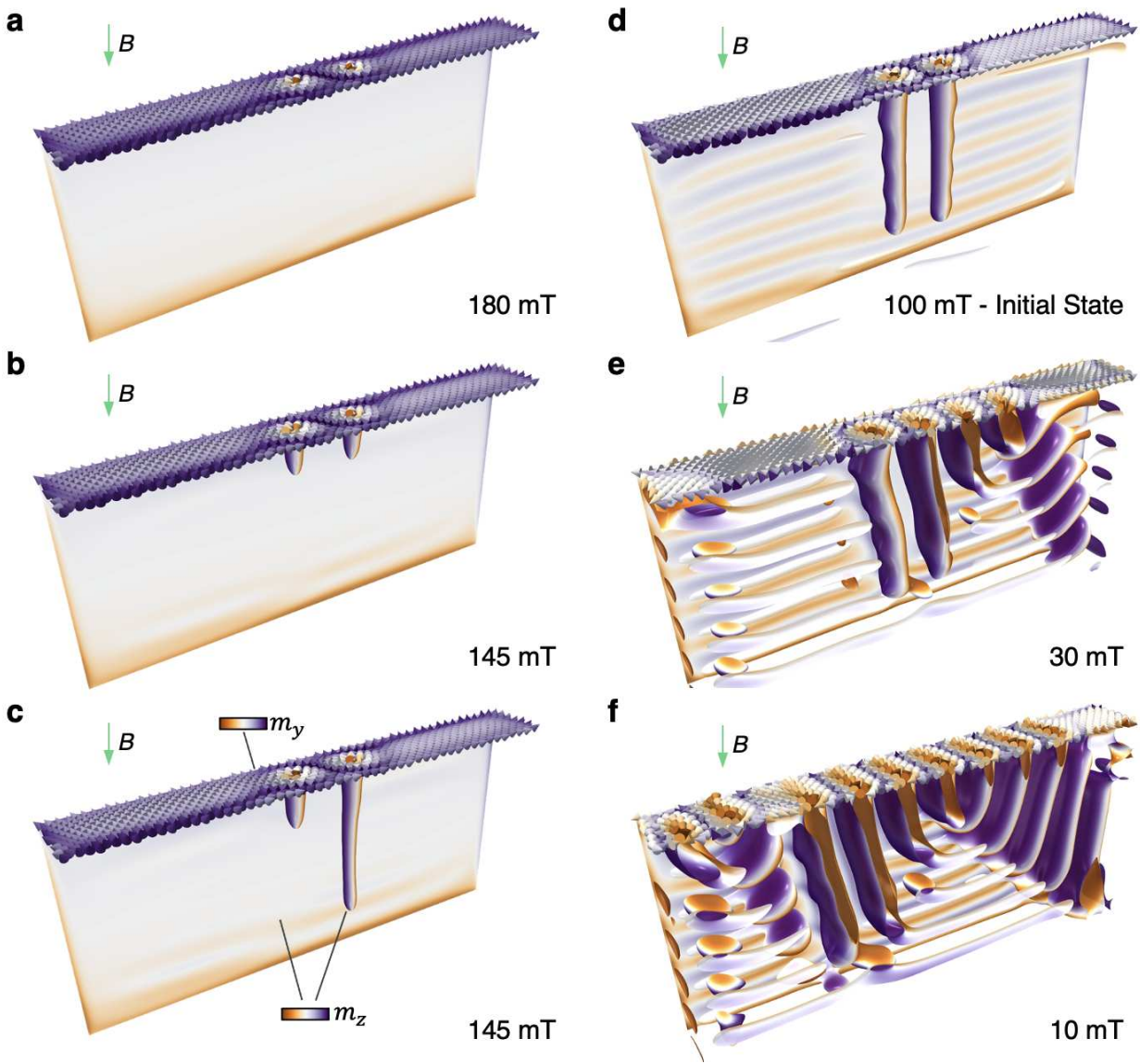


Extended Data Figure 4 | **Zero field-cooled and field-cooled data.** **a-f**, Scanning transmission x-ray microscopy images of the nanowire sample, acquired as a function of increasing in-plane field starting from 0 mT after an initial zero field-cooling (ZFC) from above  $T_C$ . The images reveal the formation of skyrmion strings in **c** from the initial helical state in **a**, as indicated by the change in spacing of the vertical contrast structures. **g-o**, Images of the nanowire acquired upon field-cooling (FC) from above  $T_C$  at a range of applied in-plane fields between 20 and 80 mT. The presence of SkSs was identified by the vertical contrast spacing. This data was utilised to create the single temperature phase diagram in Fig. 2c of the main text. The colourmap indicates the out-of-plane magnetisation  $m_z$ . The scale bar is 500 nm.

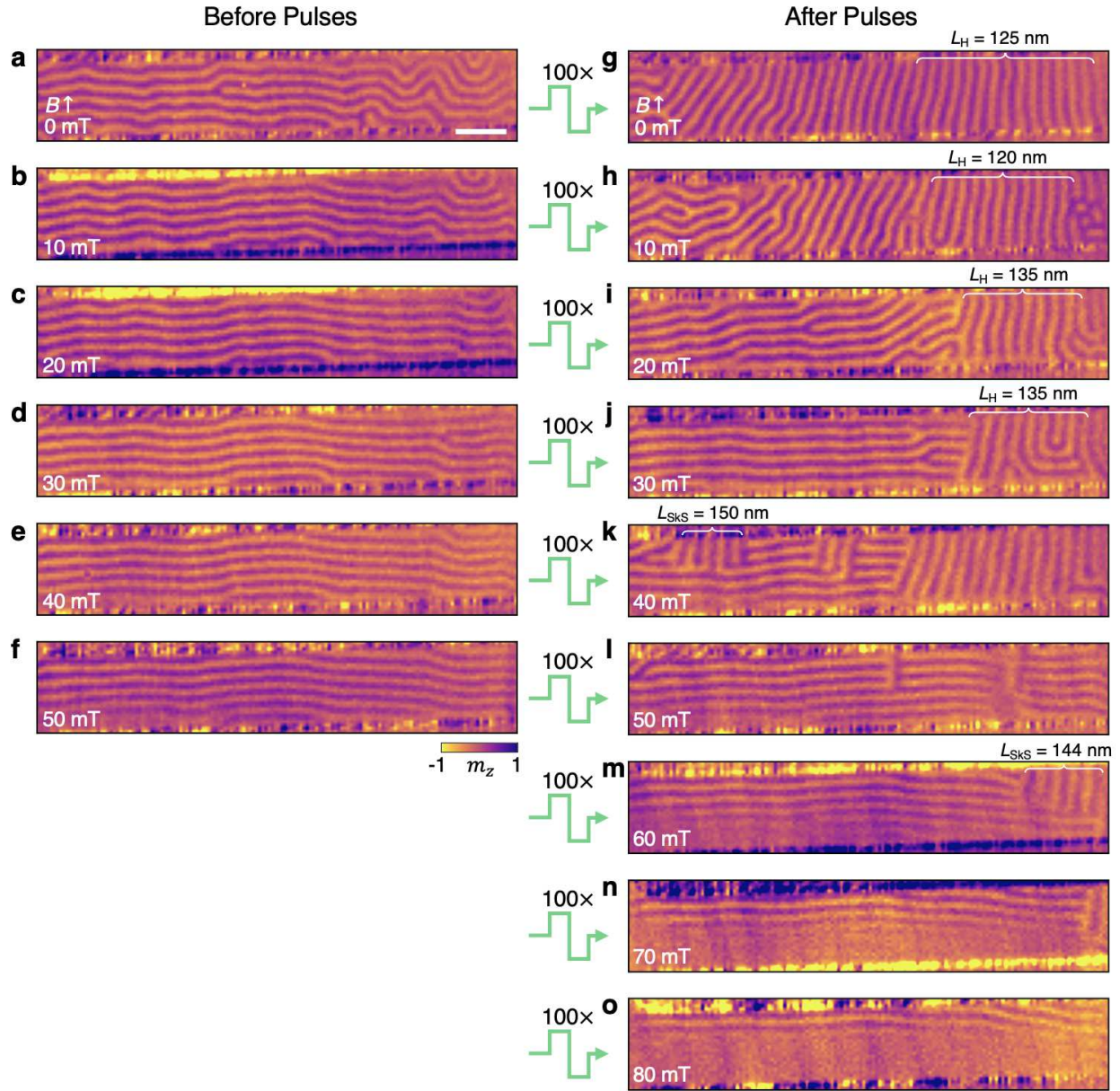




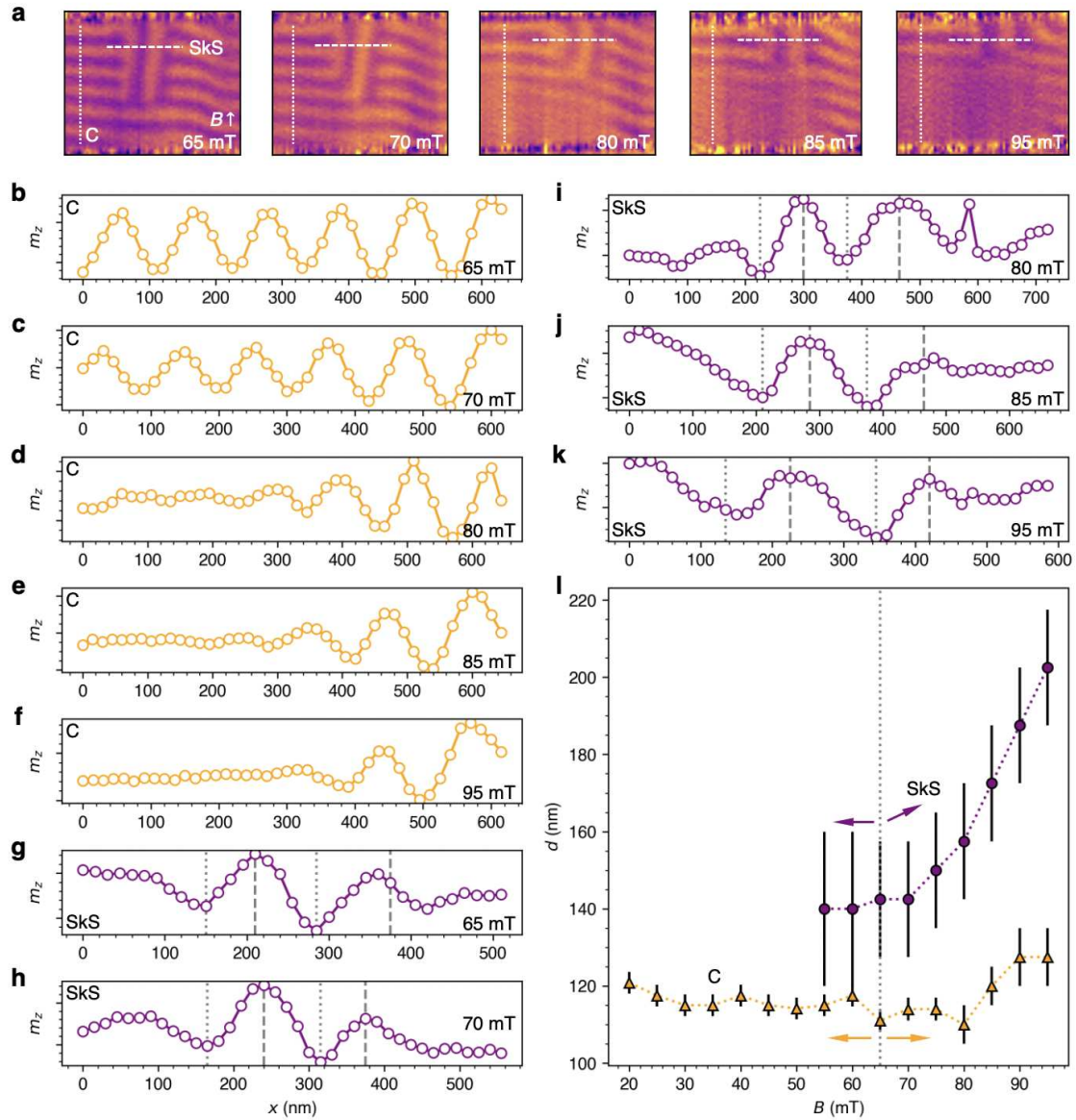
Extended Data Figure 6 | **Visualisations of the simulated separated skyrmion string field sweep.** **a-f**, Three dimensional visualisations of the magnetic configurations simulated for the two separated skyrmion string (SkS) state. The images were achieved by plotting contours showing regions where the local value of  $m_y = 0$ . The state initialised and relaxed at 100 mT is shown in **b**. From this starting point, the applied magnetic field was increased or decreased, and the system was once again relaxed, resulting in the configurations shown. For lower applied fields, the SkSs transform into the helical domain state. The colour maps label the local orientation of the magnetisation, as indicated by the colour bars.



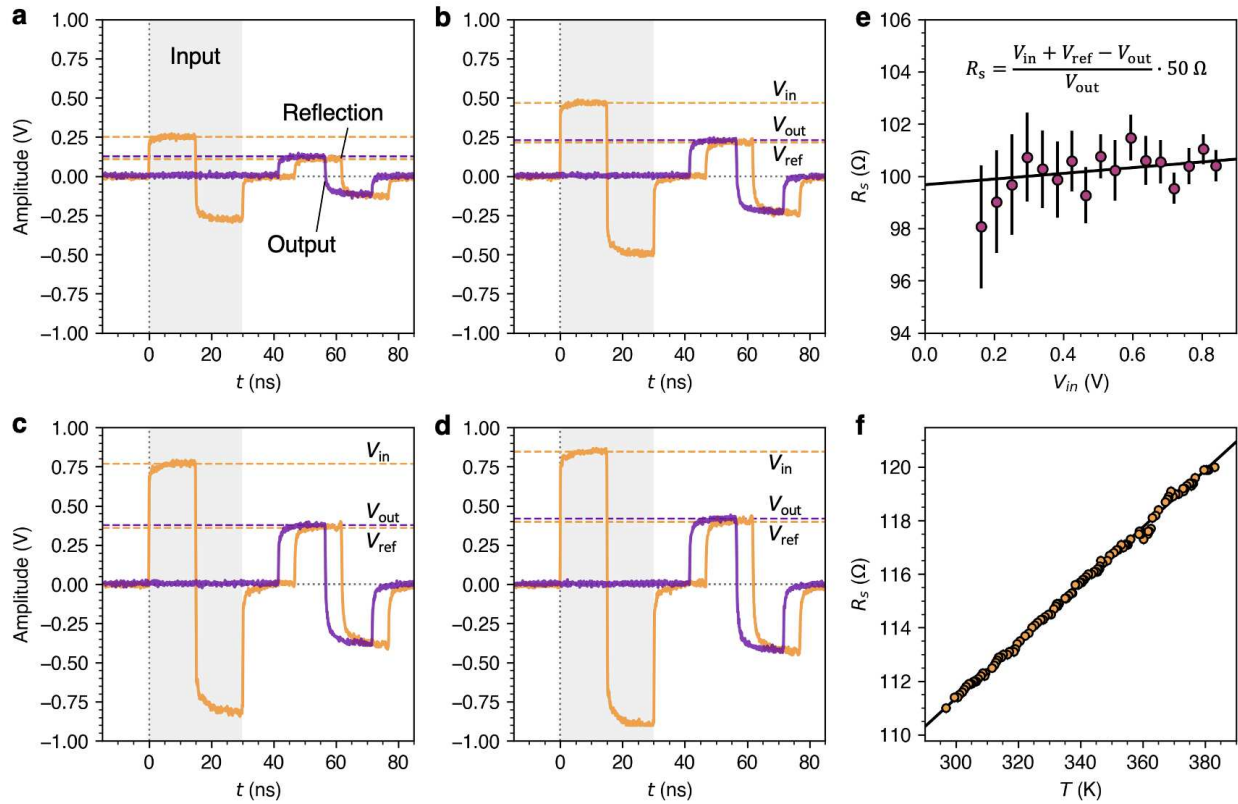
Extended Data Figure 7 | **Visualisations of the simulated adjacent skyrmion string state.** **a-f**, Three dimensional visualisations of the magnetic configurations simulated for the two separated skyrmion string (SkS) state. The images were achieved by plotting contours showing regions where the local value of  $m_y = 0$ . The state initialised and relaxed at 100 mT is shown in **d**. From this starting point, the applied magnetic field was increased or decreased, and the system was once again relaxed, resulting in the configurations shown. For higher applied fields, the SkSs unwind along their length to form the chiral bobber state at the surface of the sample. The colour maps show the local orientation of the magnetisation, as indicated by the colour bars.



Extended Data Figure 8 | **Nucleating skyrmion strings with current pulses.** **a-f**, Scanning transmission x-ray microscopy images of the nanowire sample, showing the formation of the conical state after resetting the sample by applying a  $-250$  mT in-plane field, and subsequently applying the field specified in each image. **g-o**, Images of the nanowire, showing the magnetic state achieved after applying 100 bipolar current pulses of duration 30 ns and with a current density of  $6 \times 10^{10}$  A/m<sup>2</sup>, as indicated by the green arrows. For low applied fields, this results in the formation of the helical state, or even out-of-plane skyrmions in **h**. However, for fields between 40 to 70 mT, skyrmion strings (SkS) are nucleated. The identity of the SkSs is verified by comparing their spacing to the winding length of the surrounding conical state. The colourmap indicates the out-of-plane magnetisation  $m_z$ . The scale bar is 500 nm.



Extended Data Figure 9 | **Conical and skyrmion string spacing determination.** **a**, Scanning transmission x-ray microscopy (STXM) images of the two adjacent skyrmion string (SkS) state as a function of increasing applied in-plane magnetic field. The dotted and dashed lines indicate  $m_z$  profiles taken through the conical (C) and SkS states, respectively. **b-f**, The  $m_z$  profiles for the C state from the STXM images in **a**. **g-k**, The  $m_z$  profiles for the SkS state from the STXM images in **a**. **l**, The average spacing of SkS (purple circles) and C (yellow triangles) states plotted as a function of the applied in-plane magnetic field, after being extracted from the data in **b-k**. The dashed line and arrows indicate the initial field upon field cooling, and the direction of the magnetic field change. Error bars indicate the error calculated due to the resolution limit, and the averaged number of measured SkS/C spacings.



Extended Data Figure 10 | **Joule heating estimation and resistance-temperature calibration.** **a-d**, Example 30 ns bipolar pulse traces, showing the input  $V_{in}$  and reflected  $V_{ref}$  signal in the first channel (orange), and the output signal  $V_{out}$  transmitted through the sample in the second channel (purple), for different input current densities. **e**, The measured sample resistance  $R_s$  as a function of  $V_{in}$ , following calculations using the equation shown. Error bars indicate the standard error determined by measurement of 10 or more pulses at each  $V_{in}$ . **f**, A measurement of the sample resistance,  $R_s$  as a function of the temperature,  $T$ , used as a calibration for the Joule heating estimate.